# ANALYSIS OF PLANAR SKIN MODEL EXPOSED TO DIPOLE ANTENNA RADIATION FEATURING THE USE OF THE MOM-MOM APPROACH

MARIO CVETKOVIĆ & DRAGAN POLJAK
Faculty of Electrical Engineering, Mechanical Engineering and Naval Architecture, University of Split, Croatia

ABSTRACT
The paper deals with high frequency dosimetry analysis of a planar skin model exposed to a dipole antenna radiating in the GHz frequency range. The thin equivalent strip of a perfect electrically conducting (PEC) center-fed antenna is based on the electric field integral equation (EFIE) formulation in the frequency domain solved by means of method of moments (MoM), while the simple planar model for high frequency assessment is based on EFIE formulation for lossy homogeneous biological body solved by the same numerical approach. The electric field obtained using the EFIE-PEC part is subsequently utilized as the incident field in the EFIE-dielectric part of the proposed model. The numerical results for the surface antenna current, the equivalent surface current, and the induced electric field on the surface of the planar model are given, as well as a comparison of several field measures obtained at the averaging surface of planar models of varying thickness and width, respectively. The results could be found useful in the development of computational dosimetry models in the assessment of exposure of humans to electromagnetic fields in the GHz frequency range.
*Keywords: planar skin model, dipole antenna radiation, electric field integral equation, method of moments, human exposure to EMF.*

## 1 INTRODUCTION

The use of computational dosimetry models in the assessment of human exposure to high-frequency electromagnetic fields (EMFs) is considered essential as the experimental validation is very difficult to perform in this frequency range. The improvement in computational methods is important basis for the development of exposure standards related to the safe use of EMFs [1]. According to International Commission on Non-Ionizing Radiation Protection (ICNIRP) [2], and IEEE C95.1. standard [3], respectively, the basic restrictions or the dosimetric reference levels in the frequency range of 6–300 GHz, are set in terms of the absorbed power density (APD), while below 6 GHz the exposure limits are specified in terms of specific absorption rate (SAR). Calculation of both SAR and APD is carried out by post-processing the results from the electromagnetic dosimetry model, i.e., the induced electric field. The subsequent thermal dosimetry models utilises the SAR or APD as inputs in order to determine the resulting temperature rise in the model of exposed biological tissue.

Various research groups within IEEE International Committee on Electromagnetic Safety (ICES) Subcommittee 6 study the effects of different averaging schemes of dosimetric quantities [4], [5]. These include different schemes for spatial averaging of the APD above 6 GHz, with averaging area of 4 $cm^2$, and 1 $cm^2$, for frequencies above 30 GHz, to correlate with the local maximum temperature increase. The initial step in this analysis is related to comparison of the area-averaged APD using planar skin models. The study in Li et al. [5] determined the IPD and APD averaged over the skin surface in the range of 10 to 90 GHz, employing various numerical approaches using uniform body and antenna models. To this end, different research group employed commercial electromagnetic solvers such as CST, HFSS, and Sim4Life, as well as a numerical research codes mainly based on the FDTD. On the other hand, the use of integral equation based techniques such as the method of

moments (MoM), the boundary element method (BEM), or hybrid methods is limited due to computational requirements related to frequency of the problem. The fully populated matrices in the GHz frequency range becomes prohibitively large to solve on typical desktop computers, unless GPU acceleration or parallel processing is employed [6].

This paper is on the use of a surface integral equation formulation and the method of moments (MoM) based approach to high frequency dosimetry [7]. A scenario with single $\lambda/2$ dipole antenna positioned in front of a planar body model is considered in this study. The antenna is modelled as a perfect electric conductor (PEC) radiating at 10 and 30 GHz. The antenna model is represented by a thin-strip that is formulated using the electric field integral equation (EFIE) for PEC. The EFIE formulation solved by means of MoM technique is utilized first to find the surface current distribution due to an applied voltage in the antenna feed [8]. From the determined antenna surface current distribution, the radiated electric field is found, representing the incident electric field in the subsequent step, where the EFIE formulation for the homogeneous penetrable scatterer (body) is used [9]. The numerical solution has been carried out using MoM, resulting in the induced electric field at the scatterer surface. Some illustrative examples for electric field induced on the planar model surface are given.

The outline of the manuscript is as follows. Following the introduction, the EFIE formulation for PEC object is briefly outlined, utilized in order to find the dipole antenna radiation. This is followed by a brief outline of the EFIE formulation for lossy dielectric biological body represented by the planar model. More details on the utilized planar models is given in the subsequent section including some remarks on the computational complexity regarding the use of said models at very high frequencies. The numerical results including the dipole antenna current distribution, the planar model equivalent current distribution, as well as the computed electric field are given in the next section, while concluding remarks are given in the final section.

## 2 MATHEMATICAL DETAILS

### 2.1 EFIE-PEC formulation for the dipole antenna

The frequency domain (FD) EFIE for perfect conductor is utilized for the dipole antenna model. The formulation is based on the application of equivalence theorem and appropriate boundary conditions at the antenna surface, leading to:

$$[-\vec{E}_1^{sca}(\vec{J})]_{tan} = [\vec{E}^{inc}]_{tan}, \tag{1}$$

where $E^{inc}$ and $E^{sca}$ denote the known incident field (related to voltage at antenna terminals) and the unknown scattered field, respectively. The scattered field can be expressed as:

$$\vec{E}^{sca} = -j\omega\vec{A} - \nabla\varphi, \tag{2}$$

where $\vec{A}$ and $\varphi$ denote the vector magnetic and the scalar electric potential, respectively, defined as:

$$\vec{A}(\vec{r}) = \mu \iint_S \vec{J}(\vec{r}\,')G(\vec{r},\vec{r}\,')dS'; \quad \varphi(\vec{r}) = \frac{1}{\varepsilon}\iint_S \rho(\vec{r}\,'), G(\vec{r},\vec{r}\,')dS', \tag{3}$$

where $\vec{J}$ and $\rho$ are surface current density and surface charge density, respectively, and $G(\vec{r},\vec{r}\,')$ denotes the Green's function for free space:

$$G(\vec{r},\vec{r}\,') = \frac{e^{-jkR}}{4\pi R}; \quad R = |\vec{r}-\vec{r}\,'|, \tag{4}$$

where $R$ denotes the distance between observation point $\vec{r}$ and source point $\vec{r}\,'$, and $k$ is free space wave number.

The surface charges from (3) can be expressed, through the continuity equation, as:

$$\rho(\vec{r}\,') = -\frac{\nabla'_S \cdot \vec{J}(\vec{r}\,')}{j\omega}. \tag{5}$$

Inserting (2) in (1), after some rearranging, results in:

$$\vec{E}^{inc} = j\omega\mu \iint_S \vec{J}(\vec{r}\,')G(\vec{r},\vec{r}\,')dS' - \frac{j}{\omega\varepsilon}\iint_S \nabla'_S \cdot \vec{J}(\vec{r}\,')\nabla G'(\vec{r},\vec{r}\,')dS', \tag{6}$$

where $\nabla'_S\cdot$ denotes the surface divergence operator.

The unknown surface current $\vec{J}$ are expanded by linear combination of basis functions such as the Rao–Wilton–Glisson (RWG) functions [8], as follows:

$$\vec{J}(\vec{r}) = \sum_{n=1}^{N} J_n \vec{f}_n(\vec{r}), \tag{7}$$

with $J_n$ denoting the unknown coefficients and $N$ denoting the number of triangles used to discretize the antenna surface $S$.

After testing with $\vec{t}_m(\vec{r})$, where $\vec{t}_m = \vec{f}_n$, followed by integration over surface $S$, the gradient from Green's function can be transfered to testing function, resulting in the integrals of the following form [10]:

$$\begin{aligned} A &= \iint_S \vec{t}_m(\vec{r}) \cdot \iint_{S'} \vec{f}_n(\vec{r}\,')G(\vec{r},\vec{r}\,')\,dS'\,dS, \\ B &= \iint_S \nabla_S \cdot \vec{t}_m(\vec{r}) \iint_{S'} \nabla'_S \cdot \vec{f}_n(\vec{r}\,')G(\vec{r},\vec{r}\,')\,dS'\,dS, \\ V &= \iint_S \vec{t}_m(\vec{r}) \cdot \vec{E}^{inc}\,dS. \end{aligned} \tag{8}$$

The resulting linear equations set can be written in the matrix form as

$$[\mathbf{Z}]_{PEC} \cdot \{\mathbf{I}\}_{PEC} = \{\mathbf{V}\}_{PEC}, \tag{9}$$

where the matrix $\mathbf{Z}$ size is $N \times N$, and the size of source vector $\mathbf{V}$ is $N$. Solving (9) leads to vector $\mathbf{I}$ with unknown coefficients $J_n$. From these coefficients, the antenna surface current $\vec{J}$ can be determined, and afterwards, the electric field can be found using:

$$\vec{E}(\vec{r}) = -j\omega\mu \iint_S \vec{J}(\vec{r}\,')G(\vec{r},\vec{r}\,')\,dS' - \frac{j}{\omega\varepsilon}\iint_S \nabla'_S \cdot \vec{J}(\vec{r}\,')G(\vec{r},\vec{r}\,')\,dS'. \tag{10}$$

### 2.2 EFIE-dielectric formulation for the planar model

The FD-EFIE for the lossy dielectric is utilized for the planar body model. The formulation is based on the use of the equivalence theorem [11] and the pertinent boundary conditions at the body surface, leading to the following:

$$\left[-\vec{E}_n^{sca}(\vec{J},\vec{M})\right]_{tan} = \begin{cases} \left[\vec{E}^{inc}\right]_{tan}, & i = 1 \\ 0, & i = 2, \end{cases} \tag{11}$$

where $E^{inc}$ represents the radiated field by a dipole antenna while $E^{sca}$ is the scattered electric field.

The tangential (*tan*) component of $E^{sca}$ can be written in terms of the equivalent current densities, namely $\vec{J}$ and $\vec{M}$, which are then expanded as a linear combination of basis functions. If the triangular elements are used to describe the body surface, $\vec{J}$ can be expanded using RWG basis functions [8], while $\vec{M}$ can be expanded by $\hat{n} \times$ RWG, as:

$$\vec{J}(\vec{r}) = \sum_{n=1}^{N} J_n \vec{f}_n(\vec{r}); \quad \vec{M}(\vec{r}) = \sum_{n=1}^{N} M_n \vec{g}_n(\vec{r}), \tag{12}$$

where $J_n$ and $M_n$ represent the coefficients to be solved for, while $N$ is the number of elements used to discretize the surface of the body.

The numerical solution of EFIE is carried out using an efficient scheme based on MoM reported in Cvetković et al. [9]. In the following, only basic steps are outlined. More details can be found in authors previous work, e.g., Cvetković et al. [12], [13].

Multiplying (11) by testing functions $\vec{f}_m$, with $\vec{f}_m = \vec{f}_n$, followed by integration over the complete body surface $S$, after some additional steps [9], the following integral equations set is obtained:

$$\sum_{n=1}^{N} \left( j\omega\mu_i A_{mn,i} + \frac{j}{\omega\varepsilon_i} B_{mn,i} \right) J_n + \sum_{n=1}^{N} \left( C_{mn,i} + D_{mn,i} \right) M_n = \begin{cases} V_m, & i = 1 \\ 0, & i = 2, \end{cases} \tag{13}$$

where $A_{mn}$, $B_{mn}$, $C_{mn}$, and $D_{mn}$ are the double surface integrals, while index $i = 1, 2$ denote the outside and inside region, with respect to body. The $m$ and $n$ labels, respectively, denote the triangles with source and observation points. The body's electrical properties are accounted via $\mu$ and $\varepsilon$ parameters, namely, permeability and permittivity.

The integral equations set (13) can be expressed compactly in the matrix form as

$$[\mathbf{Z}] \cdot \{\mathbf{I}\} = \{\mathbf{V}\}, \tag{14}$$

where the size of system matrix $\mathbf{Z}$ is $2N \times 2N$, while the size of source vector $\mathbf{V}$ is $2N$. It should be noted that matrix $\mathbf{Z}$ is fully populated [7]. The unknown coefficients $J_n$ and $M_n$ are determined by the solution of (14), and are used to calculate the equivalent surface electric and magnetic currents, $\vec{J}$ and $\vec{M}$, respectively.

The electric field inside and on the body surface is thus easily determined, from the equivalent surface currents, using the following:

$$\begin{aligned} \vec{E}_2(\vec{r}) = -j\omega\mu_2 \iint_S \vec{J}(\vec{r}\,')G_2(\vec{r}, \vec{r}\,')\, dS' - \frac{j}{\omega\varepsilon_2} \iint_S \nabla'_S \cdot \vec{J}(\vec{r}\,')G_2(\vec{r}, \vec{r}\,')\, dS' - \\ - \iint_S \vec{M}(\vec{r}\,') \times \nabla G_2(\vec{r}, \vec{r}\,')\, dS'. \end{aligned} \tag{15}$$

Likewise, the magnetic field can be calculated. Both fields, determined at the body surface, can be latter utilized in the calculation of absorbed power density, using one of two definitions [4], [5]:

$$S_{ab_1}(\vec{r}) = \frac{1}{2A} \iint_A \int_{z_1}^{z_2} \sigma(\vec{r}) |\vec{E}(\vec{r})|^2\, dz\, dA, \tag{16}$$

Table 1: Model dimensions, number of RWG elements $N$, number of tetrahedras (Tetra), matrix fill time $T_{fill}$, and memory allocation for system matrix $[Z]$.

| Model | Size ($cm^3$) | $N$ | Tetras | $T_{fill}$ (days:h:min) | $[Z]$ (MB) |
|---|---|---|---|---|---|
| #1 | 1 cm × 1 cm × 0.1 cm | 720 | 960 | 01:17 | 35 MB |
| #2 | 1 cm × 1 cm × 0.2 cm | 840 | 1038 | 01:46 | 52 MB |
| #4 | 1 cm × 1 cm × 0.4 cm | 1080 | 1698 | 02:55 | 94 MB |
| #5 | 1 cm × 1 cm × 0.5 cm | 1200 | 2058 | 3:41 | 118 MB |
| #10 | 1 cm × 1 cm × 1 cm | 1800 | 3182 | 9:14 | 271 MB |
| #4x1.2 | 1.2 cm × 1.2 cm × 0.4 cm | 1440 | 1982 | 5:35 | 167 MB |
| #4x1.6 | 1.6 cm × 1.6 cm × 0.4 cm | 2304 | 3495 | 17:10 | 421 MB |
| #4x1.8 | 1.8 cm × 1.8 cm × 0.4 cm | 2808 | 4303 | 1d:03:09 | 621 MB |
| #4.x2.0 | 2 cm × 2 cm × 0.4 cm | 3360 | 5268 | 1d:18:44 | 880 MB |
| #4x3.0 | 3 cm × 3 cm × 0.4 cm | 6840 | 11718 | 10d:07:16 | 3.55 GB |

where $\sigma$ is the conductivity, or a more rigorous definition [5]:

$$S_{ab_2}(\vec{r}) = \frac{1}{2A} \iint_A \Re \left[ \vec{E}(\vec{r}) \times \vec{H}^*(\vec{r}) \right] \cdot d\vec{A}, \tag{17}$$

where $\vec{E}$ and $\vec{H}$ represent the peak value of electric field and magnetic field, respectively, on the body surface, $\Re$ is the field real part and $(^*)$ denotes the complex conjugate. It should be noted that the control surface of area $A$ should be sufficiently larger than the EM penetration depth $\delta$ [4].

## 3 PLANAR SKIN MODELS

Various exposure scenarios have been considered in Li et al. [5], including a single-layer skin model whose dimensions (in mm) were $W \times H \times L = 200 \times 200 \times 100$, and $W \times H \times L = 150 \times 150 \times 75$, at 10 GHz and 30 GHz, respectively. If the conventional MoM is used, the computational size of the problem at these frequencies becomes a limiting factor [6]. Table 1 shows computational requirements for the considered models.

Let us consider e.g., a full scale planar model at 10 GHz [5]. Taking into account that element size should be on the order of $\lambda/10$, at 10 GHz, this translates to 3 mm maximum triangle side, and 1 mm at 30 GHz. Tesselating the surface with structured mesh results in the smallest number of elements equal to 225.000 triangles. This in turn results in $N = 375.000$ RWG elements, i.e., a fully populated matrix whose size is $(2N)^2$. Using a fairly decent laptop computer, featuring 4 cores for parallel computation, the computation time in case of $N = 3360$ RWG elements, according to Table 1, takes around 42 hours.

We are thus interested to find out whether the use of the reduced planar models, as shown in Fig. 1, could still be utilized, facilitating the use of conventional MoM.

We consider averaging over 1 $cm^2$ square area, employing models with varying thickness and width, as shown in Fig. 1, whose parameters are given in Table 2.

The geometry of the problem is depicted in Fig. 2.

Several locations of dipole antenna are considered, i.e., distance $d = 5, 10, 15$ mm with respect to the planar body.

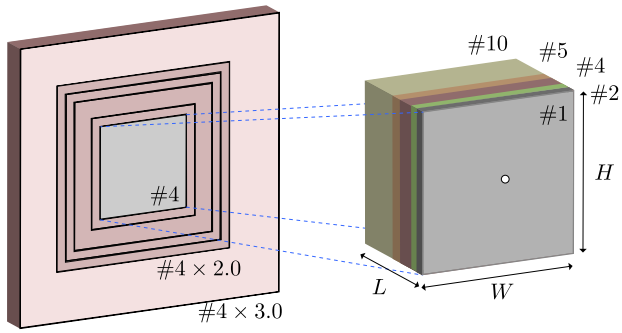


Figure 1: Used planar skin models. Models denoted $\#1 - \#10$ with different thickness $L$, while models $\#4 - \#4x3.0$ are with different front surface area. Dimensions $(W \times H \times L)$ are given in Table 1.

Table 2: Parameters of planar skin models.

| | $\sigma$ | $\varepsilon_r$ | $\delta$ | $\lambda/10$ |
|---|---|---|---|---|
| | (S/m) | | (mm) | (mm) |
| 10 GHz | 8.84 | 32.41 | 3.79 | 3 |
| 30 GHz | 27.31 | 16.63 | 0.85 | 1 |

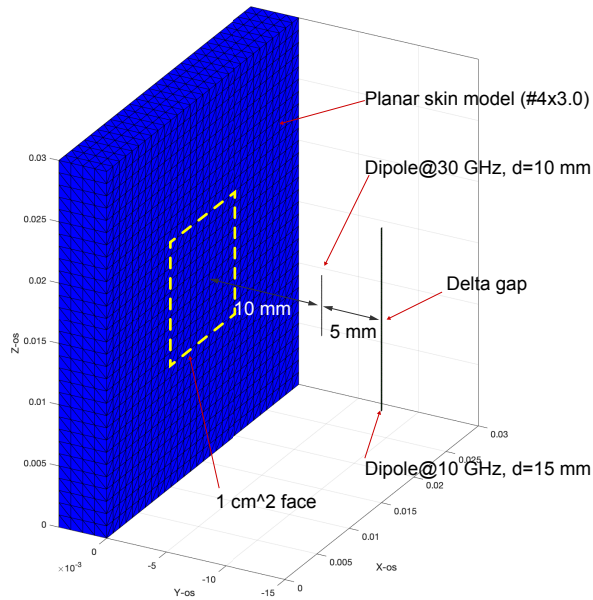


Figure 2: Geometry of the problem. Example of 30 GHz and 10 GHz halfwave dipoles, positioned 10 mm and 15 mm, respectively, in front of the planar model $\#4 \times 3.0$. Dotted square denotes 1 cm$^2$ area where averaging is carried out.

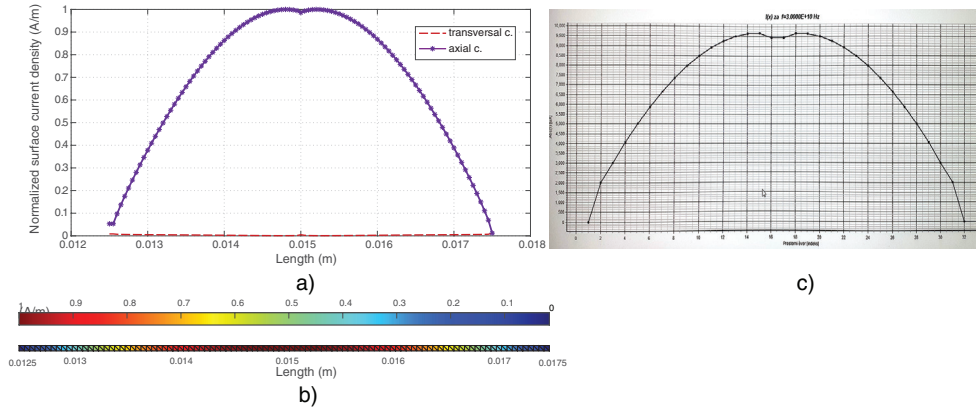


Figure 3: Example for 30 GHz halfwave dipole, dipole length $L = \lambda/2 = 5$ mm. (a) Distribution of transversal and axial component of surface current along dipole length; (b) Normalized current distribution along dipole represented by thin strip of triangular elements; and (c) Axial current obtained using SuZaNa numerical code [16].

## 4 NUMERICAL RESULTS

Some illustrative examples are presented in this section. The computational results are obtained using the EFIE formulation for PEC (antenna) and dielectric (body), respectively.

### 4.1 Dipole antenna surface current distribution

The antenna represented by thin strip of triangular elements is center-fed where the concept of delta gap is used [14]. The ideal voltage generator across a small gap is connected, assuming a gap of negligible width, thus easily implementable with RWG elements [15].

Both axial and transversal components of the antenna surface currents are depicted in Fig. 3(a).

Note the several orders of magnitude higher axial current component compared to the transversal one.

The comparison between EFIE-PEC formulation and the SuZaNa numerical code [16], as depicted in Figs 3(a) and (c), shows an excellent agreement.

### 4.2 Planar model equivalent surface currents

From the antenna current, the radiated field at any point can be calculated. If the radiated antenna field is used as the incident field in the subsequent EFIE-dielectric formulation, the equivalent electric and magnetic currents induced on the surface of planar body, can be determined, as depicted in Figs 4 and 5.

Figs 4 and 5 illustrates similar distribution of equivalent currents obtained using models of varying thickness and width, respectively.

### 4.3 Induced electric field

The induced electric field at the planar model surface can be calculated from the equivalent surface currents. An example of the numerical results for the electric field obtained at the surface of planar skin models with varying thickness is given in Fig. 6.

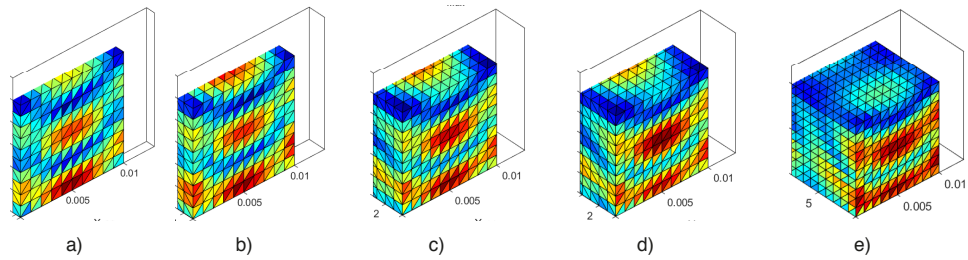


Figure 4: Distribution of equivalent electric current on the surface of planar models with varying thickness. Models at $d = 10$ mm distance to 30 GHz $\lambda/2$ dipole. (a) $\#1$; (b) $\#2$; (c) $\#4$; (d) $\#5$; and (e) $\#10$.

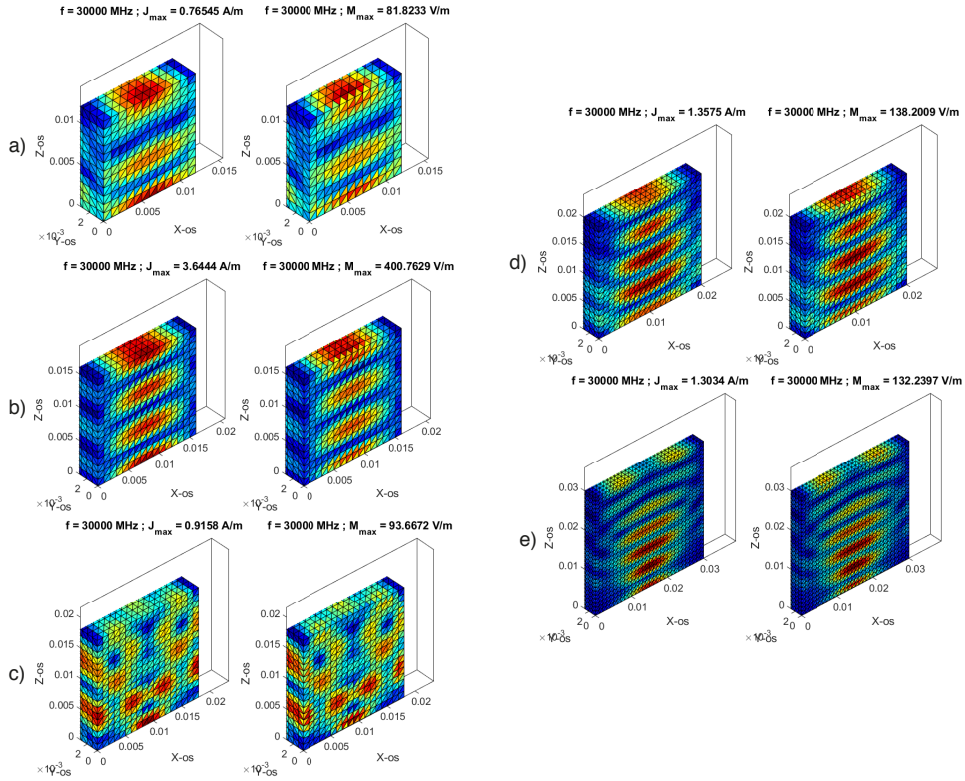


Figure 5: Equivalent electric currents and magnetic currents, respectively, on the surface of planar models with varying width. All models placed at $d = 10$ mm distance to 30 GHz $\lambda/2$ dipole. (a) $\#4 \times 1.2$; (b) $\#4 \times 1.6$; (c) $\#4 \times 1.8$; (d) $\#4 \times 2.0$; and (e) $\#4 \times 3.0$.

The authors' previous analysis of the use of planar skin models in high frequency plane wave exposure scenario has been carried out in Cvetković and Poljak [17]. The study in Cvetković and Poljak [17] showed that the reduced planar models with smaller thickness

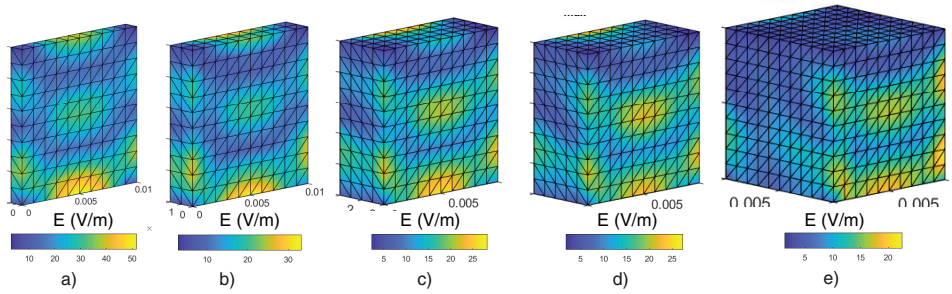


Figure 6: Induced electric field on the surface of planar models with varying thickness. Models at $d = 10$ mm distance to 30 GHz $\lambda/2$ dipole. (a) #1; (b) #2; (c) #4; (d) #5; and (e) #10.

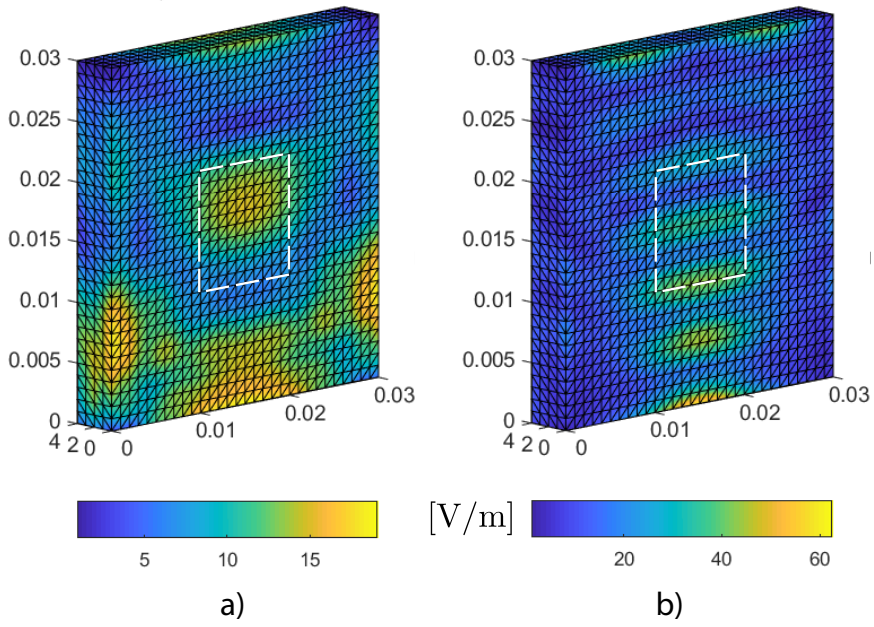


Figure 7: Electric field induced at the surface of planar model $\#4 \times 3.0$ due to $\lambda/2$ dipole at (a) 10 GHz; and (b) 30 GHz, placed at $d = 10$ mm distance. Dotted lines represent the 1 cm$^2$ averaging area.

could be utilized at 10 GHz, while at 30 GHz it is less obvious. Hence, a subsequent analysis of planar model depicted at Fig. 6(c) is carried out to study the effects of varying model widths.

### 4.4 Averaging surface area

The results for induced electric field at two frequencies of interest are shown in Fig. 7.

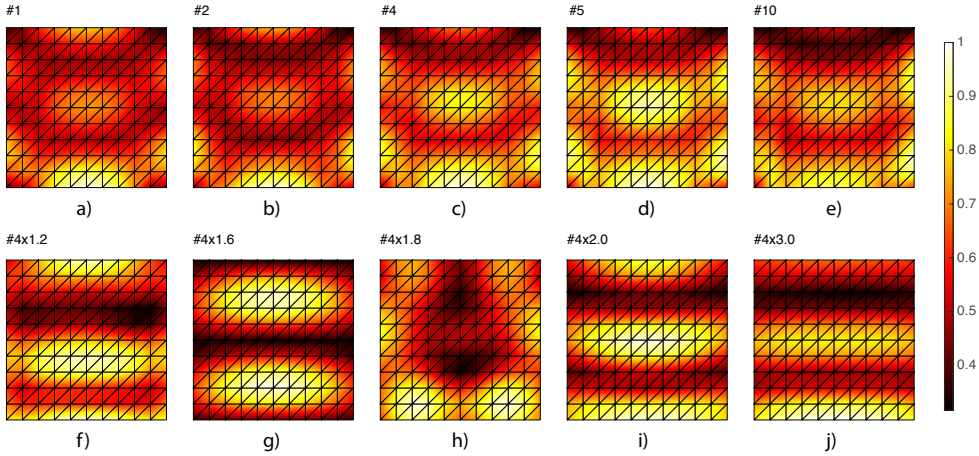


Figure 8: Normalized induced electric field at the 1 cm$^2$ averaging area obtained using planar models with varying thickness (a)–(e), and varying width (f)–(j). Example for 30 GHz $\lambda/2$ dipole.

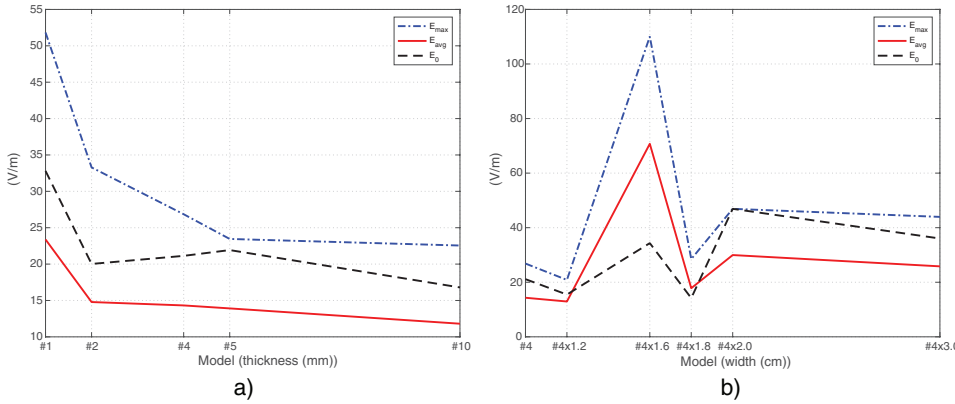


Figure 9: Dependence of several field measures from the averaging area on (a) model thickness; and (b) model width. Dotted line represents the maximum electric field ($E_{max}$), full line the averaged electric field ($E_{avg}$), and dashed line the electric field at the center point ($E_0$). Example for 30 GHz $\lambda/2$ dipole.

As depicted in Fig. 7, the dotted line representing the 1 cm$^2$ averaging area is considered when comparing models of varying thickness. The normalized distribution of the induced electric field on the 1 cm$^2$ surface averaging area is given in Fig. 8.

As evident from Fig. 8, generally similar field distribution is obtained using models with similar width or similar thickness, respectively. However, there are still some discrepancies, as evident e.g., for model $\#4 \times 1.8$.

More detailed comparison between used models can be found in Fig. 9, where dependence of several electric field measures from the averaging area is considered with respect to model thickness and width.

Generally, convergence of all measures are evident with the increasing model thickness (Fig. 9(a)). Compared to this, with the exception of model $\#4 \times 1.8$ results, the increase in model width results in the increase of all field measures considered on the 1 $cm^2$ surface averaging area.

## 5 CONCLUSION

The paper presented the analysis of planar skin models exposed to dipole antenna radiation in the GHz frequency range. The antenna model is based on frequency domain EFIE formulation for perfect electrically conducting body solved by means of MoM. The planar body model is based on the frequency domain EFIE formulation for homogeneous dielectric body also solved by MoM. The two models are coupled via antenna radiating electric field representing the incident field in the body model. Several numerical results were presented, including the antenna electric current, the body equivalent electric and magnetic currents, respectively, and the induced electric field at the surface of planar model. Several planar model geometries were considered. The averaging of electric field results in models with varying thickness and width showed similar field distributions. The follow-up study will be related to comparison of both SAR and APD metrics on the utilized planar models.

## REFERENCES

[1] Hirata, A. et al., Assessment of human exposure to electromagnetic fields: Review and future directions. *IEEE Transactions on Electromagnetic Compatibility*, **63**(5), pp. 1619–1630, 2021.
[2] ICNIRP, Guidelines for limiting exposure to electromagnetic fields (100 kHz to 300 GHz). *Health Physics*, **118**(5), pp. 483–524, 2020.
[3] IEEE, IEEE Standard for safety levels with respect to human exposure to electric, magnetic, and electromagnetic fields, 0 Hz to 300 GHz. *IEEE Std C951-2019*, pp. 1–312, 2019.
[4] Li, K. et al., Intercomparison of calculated incident power density and temperature rise for exposure from different antennas at 10–90 GHz. *IEEE Access*, **9**, pp. 151654–151666, 2021.
[5] Li, K. et al., Calculated epithelial/absorbed power density for exposure from antennas at 10–90 GHz: Intercomparison study using a planar skin model. *IEEE Access*, **11**, pp. 7420–7435, 2023.
[6] Cvetković, M., Lojić Kapetanović, A., Poljak, D. & Dodig, H., On the applicability of numerical quadrature for double surface integrals at 5G frequencies. *Journal of Communications Software and Systems*, **18**(1), pp. 42–53, 2022.
[7] Poljak, D. & Cvetkovic, M., *Human Interaction with Electromagnetic Fields: Computational Models in Dosimetry*, Academic Press, 2019.
[8] Rao, S., Wilton, D.R. & Glisson, A., Electromagnetic scattering by surfaces of arbitrary shape. *IEEE Transactions on Antennas and Propagation*, **30**(3), pp. 409–418, 1982.
[9] Cvetković, M., Poljak, D. & Hirata, A., The electromagnetic-thermal dosimetry for the homogeneous human brain model. *Engineering Analysis with Boundary Elements*, **63**, pp. 61–73, 2016.
[10] Cvetkovic, M. & Poljak, D., Electromagnetic dosimetry based on EFIE formulation and RWG basis function. *Boundary Elements and other Mesh Reduction Methods XLI*, **122**, p. 143, 2019.
[11] Cvetković, M. & Poljak, D., Surface equivalence principle and surface integral equation (SIE) revisited for bioelectromagnetics application. *Boundary Elements and Other Mesh Reduction Methods*, p. 227, 2018.

[12] Cvetković, M., Poljak, D. & Haueisen, J., Analysis of transcranial magnetic stimulation based on the surface integral equation formulation. *IEEE Transactions on Biomedical Engineering*, **62**(6), pp. 1535–1545, 2015.
[13] Cvetković, M., Šušnjara, A. & Poljak, D., Deterministic–stochastic modeling of transcranial magnetic stimulation featuring the use of method of moments and stochastic collocation. *Engineering Analysis with Boundary Elements*, **150**, pp. 662–671, 2023.
[14] Balanis, C.A., *Antenna Theory: Analysis and Design*, John Wiley & Sons, 2016.
[15] Makarov, S.N., *Antenna and EM Modeling with MATLAB*, Wiley Inc., 2002.
[16] Poljak, D., Dorić, V. & Antonijević, S., *Computer Modeling of Wire Antennas*, Kigen doo, veljača, 2009 (in Croatian).
[17] Cvetković, M. & Poljak, D., On the use of planar skin models in high frequency dosimetry assessment. Accepted for presentation at the URSI GASS 2023, Sapporo, Japan, 19–26 Aug. 2023.